NANO LETTERS
Letter
Cite This: Nano Lett. 2019, 19, 8216−8224
pubs.acs.org/NanoLett

Observation of Anisotropic Strain-Wave Dynamics and Few-Layer Dephasing in MoS_2 with Ultrafast Electron Microscopy

Yichao Zhang and David J. Flannigan*

Department of Chemical Engineering and Materials Science, University of Minnesota, 421 Washington Avenue SE, Minneapolis, Minnesota 55455, United States

Supporting Information

ABSTRACT: The large elastic strains that can be sustained by transition metal dichalcogenides (TMDs), and the sensitivity of electronic properties to that strain, make these materials attractive targets for tunable optoelectronic devices. Defects have also been shown to influence the optical and electronic properties, characteristics that are especially important to understand for applications requiring high precision and sensitivity. Importantly, photoexcitation of TMDs is known to generate transient strain effects but the associated intralayer and interlayer low-frequency (tens of GHz) acoustic-phonon modes are largely unexplored, especially in relation to defects common to such materials. Here, with femtosecond electron imaging in an ultrafast electron microscope (UEM), we directly observe distinct photoexcited strain-wave dynamics specific to both the *ab* basal planes and the principal *c*-axis crystallographic stacking direction in multilayer 2H-MoS_2, and we elucidate the microscopic interconnectedness of these modes to one another and to discrete defects, such as few-layer crystal step edges. By probing 3D structural information within a nanometer−picosecond 2D projected UEM image series, we were able to observe the excitation and evolution of both modes simultaneously. In this way, we found evidence of a delay between mode excitations; initiation of the interlayer (*c*-axis) strain-wave mode precedes the intralayer (*ab* plane) mode by 2.4 ps. Further, the intralayer mode is preferentially excited at free basal-plane edges, thus suggesting the initial impulsive structural changes along the *c*-axis direction and the increased freedom of motion of the MoS_2 layer edges at terraces and step edges combine to launch in-plane strain waves at the longitudinal speed of sound (here observed to be 7.8 nm/ps). Sensitivity of the *c*-axis mode to layer number is observed through direct imaging of a picosecond spatiotemporal dephasing of the lattice oscillation in discrete crystal regions separated by a step edge consisting of four MoS_2 layers. These results uncover new insights into the fundamental nanoscale structural responses of layered materials to ultrafast photoexcitation and illustrate the influence defects common to these materials have on behaviors that may impact the emergent optoelectronic properties.

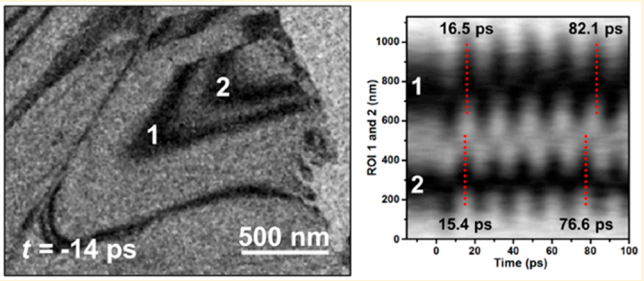

KEYWORDS: *Transition metal dichalcogenides, photoinduced strain, ultrafast electron microscopy, in situ TEM, phonons*

Modulation of bond lengths and orbital overlap in semiconducting transition metal dichalcogenides (TMDs) produces an associated variation in the electronic band configuration. While this is also true of other types of materials, the structural anisotropy of TMDs arising from a combination of relatively strong bonding in the *ab* plane and weak bonding along the *c*-axis layer-stacking direction allows for substantial elastic deformation prior to the onset of plasticity in few to monolayer specimens.[1,2] Accordingly, both the electronic and the optical properties of these materials can be tuned over a relatively wide range of energies via the presence of strain, be it tensile, compressive, shear, or torsional (i.e., layer twisting).[3−10] Indeed, although elastic deformations in excess of 10% the initial dimensions can be sustained, applied strains of a few percent can produce bandgap shifts of hundreds of millielectron volts.[5,6,10−12] Fundamental properties such as these have triggered vigorous investigation into potential device applications.[13] For example, both multilayer and monolayer TMDs have been investigated as hosts of strain-inducing defects, especially along exposed basal-plane edges, for single-photon emission, making such systems potential candidates for applications in quantum computing and adaptable precision optoelectronics.[14−17]

Sensitivity of the electronic density of states in TMDs to structural deformation, combined with the role of structural imperfections in emergent photonic properties, leads to questions pertaining to how photoexcitation might modulate the crystal lattice and the nanoscale morphology. Indeed, structural responses resulting from photoexcitation produce both local and global variations of the intralayer and interlayer bonding, as revealed with optical, electron, and X-ray scattering methods.[18−28] For example, in monolayer MoS_2 electron−

Received: August 30, 2019
Revised: October 12, 2019
Published: October 28, 2019

DOI: 10.1021/acs.nanolett.9b03596
Nano Lett. 2019, 19, 8216−8224

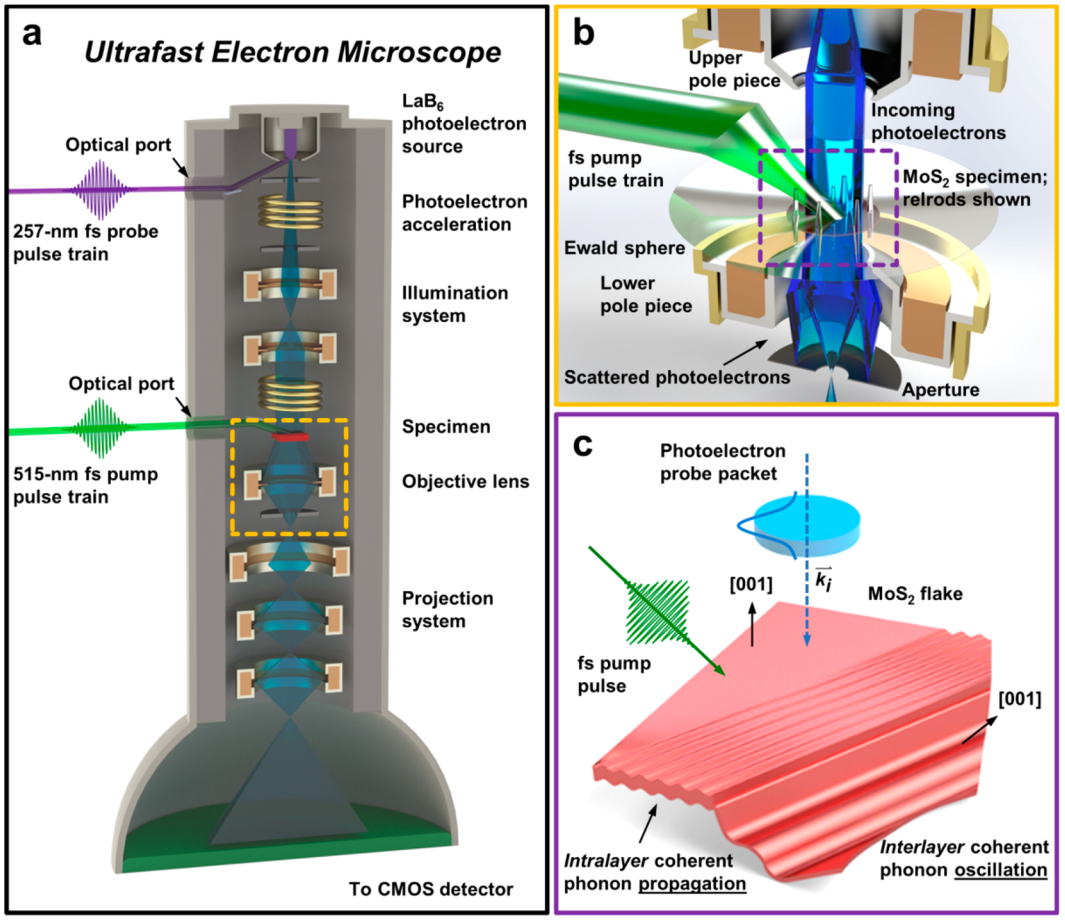

Figure 1. UEM and experimental configuration. (a) Simplified schematic of the UEM (not to scale) with key features and components labeled. The dashed yellow box highlights the specimen and objective-lens region shown in (b). (b) Magnified view of the specimen and objective-lens region in the UEM with key features and components labeled. Note that a portion of the Ewald sphere and the reciprocal-lattice rods (relrods) are shown simply for illustrative purposes. The position of the aperture with respect to the scattered photoelectrons is meant to illustrate that the imaging condition is bright field. The dashed purple box highlights the specimen region shown in (c). (c) Illustration of the configuration of the MoS_2 specimen studied here with respect to the incident laser pump pulses and photoelectron probe packets. Note that the specimen is configured such that both the *ab* plane and the *c*-axis stacking direction are accessible with a single incident photoelectron wave vector, as denoted by the relative orientation of the two [001] zone axes. This enables capture of both intralayer and interlayer strain-wave dynamics within a single UEM image series.

lattice thermalization and subsequent dynamic ripple formation having 1 Å heights and 2.5% associated peak strains occur within 2 ps of femtosecond (fs) photoexcitation, as determined via variations in Bragg-spot intensities and widths in ultrafast electron diffraction measurements.[20] In more recent fs X-ray diffraction studies of mechanically exfoliated multilayer 2H-MoS_2, the specific material of focus here, it was reported that photoexcitation produces an initial *c*-axis *compression* occurring within the first 20 ps attributed to modulation of the interlayer van der Waals bonding.[24] The optically driven compression was reported to precede thermal effects, which manifest as excitation of a coherent, low-frequency interlayer mode following the initial compression. The overall behaviors were correlated to the relatively long carrier lifetimes in the indirect-gap multilayer material. This was supported by observation of fluence-dependent effects, where the electronic and thermal contributions to the observed dynamics become comparable at a laser fluence of 0.1 mJ/cm^2 for above-gap photoexcitation.

The precise nature of initial and subsequent photoinduced structural dynamics are influenced by a number of factors, such as the boundary conditions, the specimen morphology, and the optical penetration depth and crystal thickness. Of particular interest here, discrete defects in the form of interfaces, grain boundaries, and step edges can act as local nucleation sites for excitation and formation of photoinduced strain waves in TMDs.[21−23] Accordingly, each discrete structural feature having dimensions that are on par with the strain-wave deformations has associated with it a particular (local) set of boundary conditions that may also measurably influence relevant emergent behaviors, depending on the overall defect density.[29−34] As such, detailed behaviors directed by local structure and morphology may remain unresolved when regions that are large relative to such features are probed. Note that although the impact of defects on the electronic and optical properties of MoS_2 has been the subject of numerous studies,[6,35−42] the microscopic interconnectedness of defects, *structural* dynamics, and emergent behaviors has received far less attention. Despite this, knowledge of such behaviors may be important for ultimately gaining strict control over strain-tunable properties and devices, especially for applications requiring high precision, accuracy, and sensitivity with small form factors.

DOI: 10.1021/acs.nanolett.9b03596
Nano Lett. 2019, 19, 8216−8224

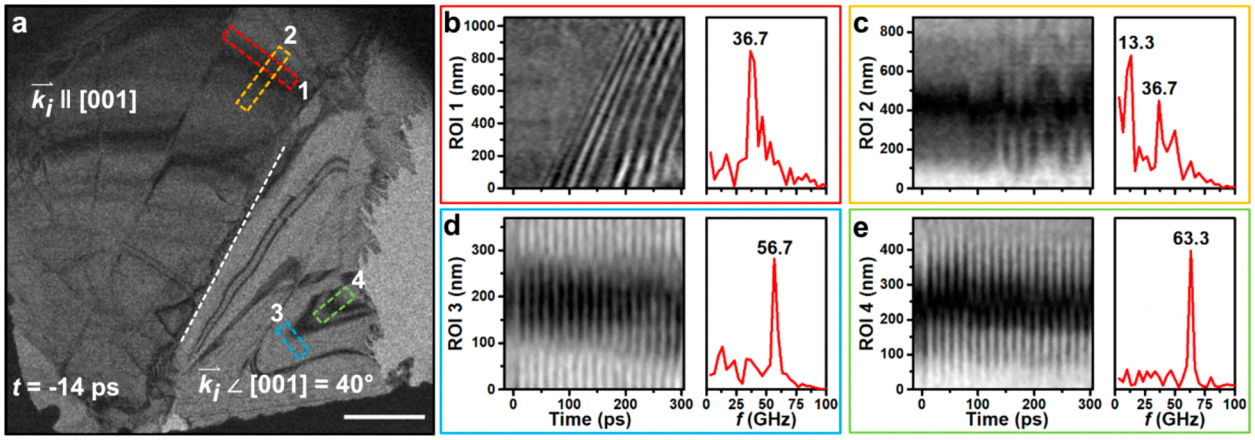

Figure 2. Localized anisotropic coherent strain-wave dynamics in MoS_2. (a) Representative UEM bright-field image of the MoS_2 specimen 14 ps prior to the first observed response ($t = -14$ ps). The white dashed line near the center of the field of view marks the approximate delineation of the two differently-oriented crystal regions. The relatively darker region generally to the left of the dashed line is the thicker crystal section oriented approximately along the [001] crystallographic direction (i.e., where the [001] zone axis is parallel to the incident electron wave vector, $\vec{k}_i$). Generally to the right is the thinner section, where the [001] zone axis is tilted 40° with respect to $\vec{k}_i$. The colored dashed rectangles mark four regions of interest (ROIs 1 through 4) within which coherent strain-wave dynamics were observed. The scale bar represents 1 μm. (b–e) Space-time contour plots (STCPs) generated from the ROIs highlighted in panel (a) along with the fast Fourier transform (FFT) of each intensity profile within the STCPs. The position of the ROI label in panel (a) marks the y-axis origin in the STCPs. The prominent frequencies within each STCP are labeled in the corresponding FFT. The gray color scale represents the averaged normalized counts, with dark representing strongly scattering regions.

Following the arguments above, resolving discrete, morphology-influenced dynamics becomes especially important in defect-laden specimens, such as mechanically exfoliated TMDs, which can be rich in structural and morphological variation, especially on atomic to nanometer-scale dimensions (e.g., point defects, terraces, step edges, layer twists, and wrinkles).[22,35,41,43−45] As such, probing dynamics in real space on relevant spatiotemporal scales is desirable for developing a comprehensive understanding of the influence of such features on photoinduced strain-wave behaviors, which include phonon excitation, strain-wave launch and propagation, and relaxation back to the ground state. Previous studies have demonstrated that such detailed behaviors in TMDs can be resolved with real-space fs electron imaging in an ultrafast electron microscope (UEM).[21−23] As an example relevant to the work reported here, UEM has been used to directly image the excitation and launch of intralayer propagating strain waves from a vacuum-crystal interface in exfoliated multilayer 2H-MoS_2.[23] Evolution and relaxation of the initial dynamics from picoseconds to microseconds was spatiotemporally resolved, revealing an intermediate transition state, characterized by incoherent dynamics, that temporally bridges the high-frequency (THz to GHz) and low-frequency (MHz) coherent responses. However, this and other studies of MoS_2 structural dynamics have yet to resolve the fundamental manner in which both the intralayer and the interlayer strain-wave modes are excited and evolve, especially in the presence of discrete structural imperfections common to such materials.

Here, using UEM fs bright-field imaging, and by accessing 3D structural information within a single 2D projected image series, we spatiotemporally resolve the photoexcitation and evolution of the interlayer mode in multilayer 2H-MoS_2 (simply MoS_2 from here forward) with respect to structural imperfections and to the intralayer propagating mode. We find evidence of initial excitation of the interlayer c-axis oscillation preceding launch of the intralayer mode by 2.4 ps, well within the time scale of reported optically driven interlayer compression and comparable to electron−phonon coupling times in MoS_2.[20,24,46] Our hypothesis is that this is indicative of initial anisotropic motion at the crystal-layer edges and along the principal c-axis layer-stacking direction and that these dynamics contribute to the preferential launch of in-plane propagating strain waves from the basal plane edges. This is supported by observation of picosecond localized dephasing of the interlayer mode driven by a structural discontinuity consisting of a crystal step edge having a four MoS_2 layer height. These particular dynamics manifest as a temporal shift in the oscillatory behavior of individual defect-delineated bend contours and arise from differing local transit times of the energetic structural displacement between the outer MoS_2 layers. Accordingly, these results illustrate the manner in which structure-directed strain-wave excitation and evolution occur at discrete, nanoscale structural features in layered materials. Additionally, the results provide new insight into the microscopic behaviors of photoexcited MoS_2, while also illustrating the usefulness of fs electron imaging for spatiotemporally resolving such effects.

All studies of dynamics were conducted in the Ultrafast Electron Microscopy Lab at the University of Minnesota.[21,47] Figure 1 contains an overview of the UEM instrument (Figure 1a), the experimental concept, and the configuration of the MoS_2 specimen (Figure 1b,c). The main pieces of instrumentation are an FEI Tecnai Femto UEM (Thermo Fisher) and a 6 W Yb/KGW fs pulsed laser (Light Conversion PHAROS). Experiments were performed in a pump−probe configuration using in situ optical pumping with 300 fs laser pulses (measured outside the UEM column with a Light Conversion GECO scanning autocorrelator) and probing with discrete photoelectron packets generated from a custom 50 μm flat, graphite-encircled LaB_6 cathode (Applied Physics Technologies). The 1 ps delays used here were controlled using a mechanical bearing linear motor stage (Aerotech,

DOI: 10.1021/acs.nanolett.9b03596
Nano Lett. 2019, 19, 8216−8224

PRO165LM), and the UEM images were acquired in a randomized fashion (i.e., the delay stage was moved randomly from time-point to time-point, and the image series was put into linear time post-experiment). All experiments were conducted with a pump (excitation) wavelength of 515 nm (2.4 eV), a laser fluence of 0.8 mJ/cm^2, an estimated Gaussian spot size of 120 μm full width at half-maximum (fwhm), and a repetition rate of 20 kHz. Both laser power and energy were measured (Newport) outside the UEM column and then estimated based on the properties of the intervening optics. Photoelectron packets were generated within the gun region of the UEM using 257 nm fs laser pulses and subsequently accelerated to 200 keV energies and directed onto the specimen for bright-field imaging using methods common to conventional transmission electron microscopy (TEM). A 40 μm diameter objective aperture was used for all UEM images in order to enhance image contrast.

The multilayer MoS_2 specimen was prepared via mechanical exfoliation from a bulk crystal (2D semiconductors) following previously reported methods and was supported on a 2000-mesh copper TEM grid (Ted Pella, G2000HS).[21,23] The specific specimen region of interest was freestanding and consisted of two differentiable crystal regions: one oriented with the principal [001] crystallographic zone axis parallel to the incident electron wave vector (i.e., $\vec{k}_i \parallel [001]$) and one tilted by 40° out of the specimen plane (i.e., $\vec{k}_i \angle [001] = 40°$). Accordingly, this configuration enabled simultaneous access to both the *ab* plane and the *c*-axis layer-stacking direction and, thus, both the intralayer and interlayer dynamics, respectively. That is, dynamics occurring both within and between the individual MoS_2 layers are captured in the 2D-projected UEM image series. Additional details can be found in the Supporting Information.

Figure 2 shows a reference UEM bright-field image of the multilayer MoS_2 specimen acquired 14 ps prior to the first observed response, along with the resulting interlayer and intralayer photoinduced strain-wave dynamics. As seen in Figure 2a, the two differently-oriented crystal sections are delineated by an approximately linear (at this magnification) crystal−crystal interface in the form of a kinked terrace. In addition to being differently oriented, the two sections differ in thickness by 51.9 ± 8.2 nm, as determined with electron energy-loss spectroscopy (EELS; see the Supporting Information and Figure S1). From the EELS measurements, the thickness of the $\vec{k}_i \parallel [001]$ section was found to be 74.9 ± 6.8 nm, while the $\vec{k}_i \angle [001] = 40°$ section was 23.0 ± 4.5 nm (errors are derived from fits to the zero-loss peak and the bulk plasmon in the spectra). In the UEM bright-field image series, photoinduced strain waves manifest as spatiotemporal oscillations of diffraction contrast, typically arising from crystal bend contours.[21−23,48−50] Upon photoexcitation, strain waves tend to propagate within the *ab* plane (intralayer) and along the *c*-axis stacking direction (interlayer).[21−24] This energetic disturbance manifests as crystal-lattice motion that modulates the local Bragg scattering condition in the immediate vicinity of the transient elastic deformation. In bright-field imaging, regions of the specimen that appear dark are strongly scattering (i.e., oriented along or nearly along the Bragg condition), whereas those that are bright are weakly scattering. Intralayer propagating strain waves are identifiable as contrast waves that travel across the field of view at the speed of sound, whereas the interlayer mode produces contrast oscillations about a fixed spatial position.[21,22,49]

Figure 2b−e displays the spatially localized behaviors of both the intralayer and interlayer photoinduced strain-wave dynamics. For the intralayer propagating mode (Figure 2b,c), contrast modulation parallel to the propagation direction is distinctly different from that of the perpendicular orientation when visualized in a space-time contour plot (STCP). The propagating portion of the wave appears as tilted contrast features, indicative of wavefront motion across a select region of interest (ROI; Figure 2b), whereas the STCP for the perpendicular portion appears as oscillatory behavior about a fixed spatial position (Figure 2c). Specifically in Figure 2, the intralayer propagation direction is parallel to the long edge of ROI 1 and perpendicular to the long edge of ROI 2 (red dashed and yellow dashed rectangles, respectively, in Figure 2a). As a result, the STCPs (Figure 2b,c) consist of tilted and vertical contrast features, respectively. For the propagating portion of the intralayer strain waves, characteristics of the tilted contrast features are dictated by wavefront velocity. Here, the speed is found to be 7.8 ± 0.3 nm/ps (temporal frequency of 36.7 GHz; error is one standard deviation of the mean of the individual speeds of five separate wavefronts). This closely matches previous experimental measurements and is in agreement with that expected from the MoS_2 elastic constants (see the Supporting Information, Figure S2 and Table S1 for additional details).[23,26,51−54] The preferential direction is given by the sign of the slope and the orientation of the ROI in the image series (here, the ROI labels in Figure 2 mark the origin of the *y*-axis in the corresponding STCPs). As previously observed in MoS_2 and other TMDs, the preferred intralayer propagation direction is generally perpendicular to and initially away from the crystal−crystal interface (here, the kinked crystal terrace).[21−23] Not unexpectedly, the 36.7 GHz temporal frequency of the intralayer propagating mode also appears in the FFT generated from the STCP of the perpendicular ROI (ROI 2; Figure 2c). In addition to this, however, a lower-frequency oscillation (13.3 GHz) absent from ROI 1 is also present. This frequency arises from excitation of the interlayer mode in this section of the crystal, as discussed below.

Unlike intralayer strain waves, the interlayer mode has no *ab*-plane propagating component. Instead, this mode consists of a coherent oscillation along the principal crystallographic *c*-axis stacking direction and is bounded by the outer MoS_2 layers. In UEM bright-field imaging, this causes a coherent oscillation of bend contours about a fixed spatial position that is most visible when the crystal section of interest is oriented away from the $\vec{k}_i \parallel [001]$ condition. Accordingly, the interlayer-mode dynamics are readily observed in the $\vec{k}_i \angle [001] = 40°$ section of the specimen studied here. Importantly, tilting away from the [001] zone axis also effectively "hides" the intralayer propagating strain waves such that the interlayer mode is visually pronounced. This is demonstrated in Figure 2d,e. The two bend contours monitored in the UEM image series (ROIs 3 and 4) both display only coherent oscillatory behaviors about a fixed spatial position and are devoid of signatures of the intralayer dynamics, as is apparent from the vertical contrast oscillations comprising the STCPs for each bend contour. This is despite the two ROIs being oriented

DOI: 10.1021/acs.nanolett.9b03596
Nano Lett. 2019, 19, 8216−8224

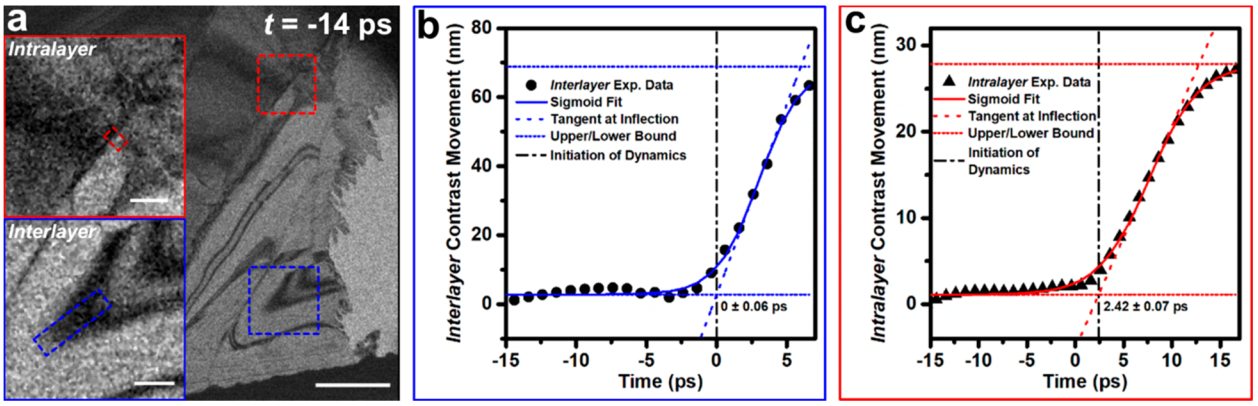

Figure 3. Spatiotemporally resolved intra- and interlayer strain-wave mode excitation in MoS_2. (a) Representative UEM bright-field image acquired 14 ps prior to the onset of contrast motion ($t = -14$ ps). The red and blue dashed boxes denote the ROIs within which intralayer and interlayer strain-wave dynamics were first observed, respectively. The scale bar represents 1 μm. The labeled insets, which show magnified views of the two ROIs, display the specific positions at which contrast dynamics were monitored (denoted by the colored dashed rectangles). The scale bars represent 200 nm. (b,c) Plots of the initial contrast movement arising from excitation of the interlayer (b) and intralayer (c) modes. Both are least-squares fit with a sigmoid function. The upper/lower bounds, as well as the tangent at the inflection points, are shown. The vertical black dot-dashed lines mark the position of the intersection of the tangent and the lower bound. The relative times are labeled in each panel near the intersection point, and the errors are derived from the fits.

perpendicular with respect to one another, as is also the case for ROIs 1 and 2 in the $\vec{k}_i \parallel [001]$ crystal section. This illustrates that one is not simply arising from the perpendicular component of a propagating intralayer mode.

As with the intralayer mode, the speed of the interlayer strain waves can be extracted from FFTs of the associated STCPs when combined with knowledge of the thickness of the specific ROI.[21,22] This general approach has also been taken in ultrafast diffraction measurements of the interlayer mode in MoS_2 and amounts to determining the time required for one round trip between the outer layers.[24] Here, combining the observed frequencies of the interlayer mode in the $\vec{k}_i \angle [001] = 40°$ crystal section (56.7 and 63.3 GHz) with the measured thickness (23 nm) returns a speed of 2.6 to 2.9 nm/ps, again consistent with previous experimental observations and as expected from the elastic constants (see the Supporting Information, Tables S2 through S4, and Figures S3 and S4).[24,51−54] The 6.6 GHz difference between the two distinct frequencies arises from a slight difference in layer number within the two ROIs. The consequences of this with respect to spatiotemporal and morphology-influenced variations in the observed dynamics are illustrated and discussed in more detail below. As mentioned above, the effect of thickness on the observed frequencies also explains the 13.3-GHz signal present in the FFT of the STCP from ROI 2; this frequency is in good agreement with that expected for the interlayer mode in this relatively thick crystal region. Observation of this mode for this particular orientation can be explained by noting that slight bending of the crystal, such that $\vec{k}_i \parallel [001]$ is not exclusively satisfied within the entire ROI, will enable observation of interlayer dynamics. See Supporting Videos 1 and 2 to view the UEM image series and a difference image series, respectively, from which the data shown in Figure 2 was generated.

As noted above, excitation of the interlayer mode in multilayer MoS_2 has been ascribed to a charge-carrier-related impulsive compression following fs photoexcitation, which was noted to precede the onset of thermal effects.[24] Accordingly, determination of the moment of excitation of the intralayer propagating mode relative to the interlayer mode, and especially in the presence of structural discontinuities, is required for developing a comprehensive understanding of the overall dynamics. Here, this was addressed by spatiotemporally identifying the initial moments of strain-wave dynamics for each mode within the same field of view and for the same UEM image series. The results of this are summarized in Figure 3. As with the data displayed in Figure 2, initial strain-wave dynamics manifest as contrast motion in the UEM image series. The initial moments of contrast motion can then be plotted as a physical distance traveled in the image series as a function of time. Because the specific condition here enables access to both modes within the 2D projected images, the initial moments of contrast motion arising from excitation of each can be directly compared to one another. This then allows for elucidation of several behaviors; including the manner in which dynamics are initiated, the precise nature of the spatiotemporal relationships between the modes, and the time scales associated with these processes. See the Supporting Information and Figure S5 for additional details.

In order to directly compare the first moments of strain-wave excitation, initial contrast motion associated with each mode was fit with a sigmoid function, and the temporal point of intersection of the lower bound and the tangent at the inflection was defined as the moment at which dynamics were initiated. This provided a consistent and unbiased means of direct comparison. The regions identified as displaying the initial contrast motion are highlighted in Figure 3a, whereas the method for determining the relative start times (i.e., the initiation of strain-wave dynamics for each mode) is illustrated in Figure 3b,c. Such an approach revealed that excitation of the interlayer mode precedes onset of the propagating intralayer mode by 2.4 ps. Note here that although the interlayer mode is not immediately discernible in the $\vec{k}_i \parallel [001]$ region, it is nonetheless excited throughout the specimen, regardless of orientation. Recall from Figure 2 that the temporal frequencies determined from the STCPs, while not precisely denoting the relative start time in that particular analysis, showed the

DOI: 10.1021/acs.nanolett.9b03596
Nano Lett. 2019, 19, 8216−8224

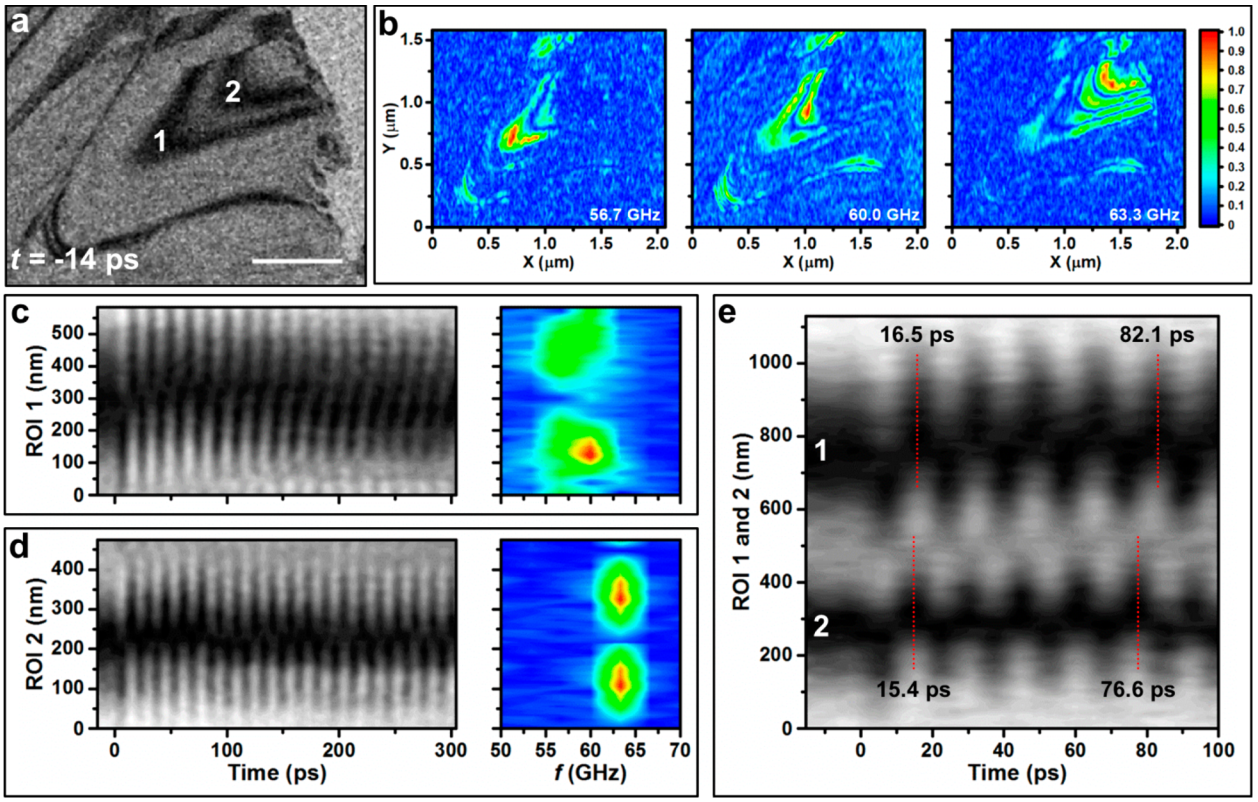

Figure 4. Few-layer dephasing of interlayer strain waves in MoS_2. (a) Representative UEM bright-field image of the $\vec{k}_i \angle [001] = 40°$ crystal section 14 ps prior to initial contrast motion ($t = -14$ ps). The two specific bend contours analyzed are labeled 1 and 2. The scale bar represents 500 nm. (b) Spatial frequency maps of the field of view shown in panel (a) at 56.7, 60.0, and 63.3 GHz (left to right). The color bar is frequency amplitude normalized to the largest value. (c,d) STCPs of the two bend contours labeled in panel (a); ROI 1 = bend contour 1, and ROI 2 = bend contour 2. The associated FFTs of the STCPs are shown to the right of the corresponding plots. (e) STCP of both bend contours in panel (a) (labeled 1 and 2) over the first 100 ps following fs photoexcitation. The first six oscillation periods are shown with the first and the fifth periods marked with red vertical dashed lines and labeled with the time at which that particular peak occurs (e.g., 16.5 ps compared to 15.4 ps for the first oscillation period of the first and second bend contour, respectively).

interlayer mode was excited in the $\vec{k}_i \parallel [001]$ region of the crystal, as indicated by the observed 13.3 GHz oscillation.

Initiation of the interlayer mode 2.4 ps before launch of the intralayer mode, together with consistent observation of in-plane strain-wave launch at the kinked crystal terrace, suggests the inherent structural anisotropy at such defects and the *c*-axis motion initiates the traveling modes in the *ab* plane. In previous work, finite element modeling of a layered structure with a discrete terrace indicated that impulsive excitation along the *c*-axis stacking direction leads to in-plane propagating modes emanating from the defect.[22] Note, however, that only a qualitative indication of the existence of a time delay between excitation of the two modes was predicted. The model also did not account for the anisotropic structural response to optical penetration depth. Further, because the finite elements were 2 nm in thickness, no conclusions could be drawn regarding the molecular-scale dynamics.

Microscopically, the behavior observed here can be described as an in-plane propagating train of ripples emanating from the terrace, initiated by a relatively large change in the *c*-axis stacking direction in the vicinity of the defect upon photoexcitation. That is, the exposed molecular layer edges of the basal planes allow for increased freedom of motion at the terrace relative to regions far from the defect, similar to observations of crystal-vacuum interfacial dynamics in MoS_2.[23] The initial shift in contrast associated with the in-plane mode arises from that particular nanoscale crystal region moving into a strongly scattering condition in response to photoexcitation, thus serving as a useful and sensitive indicator of the first moments of motion.[50] The apparent delay of 2.4 ps indicates that only a portion of the crystal along the depth has responded to the initial excitation in that time, which is expected owing to the thickness and the optical penetration depth of MoS_2 for 2.4 eV photons. Because the speed of sound along the *c*-axis direction is approximately 3 nm/ps, the structural perturbation associated with this mode will have propagated 7 nm in 2.4 ps, which is approximately 10% and 30% of the total thickness of the thick and thin regions, respectively. Thus, the initial contrast motion associated with the in-plane mode is hypothesized to be indicative of the first moments of propagating ripple formation triggered preferentially at the crystal terrace by the enhanced basal-plane edge freedom of motion along the *c*-axis direction. Note that these particular results do not directly provide additional insight into previously reported initial interlayer compression following fs photoexcitation in multilayer and bilayer MoS_2.[24,55] Thus, care was taken not to ascribe the initial *c*-axis motion to either a compression or an expansion, though either could cause the particular contrast dynamics observed here.

The results shown in Figure 3 suggest the particular interlayer dynamics that occur may be sensitively dependent

DOI: 10.1021/acs.nanolett.9b03596
Nano Lett. 2019, 19, 8216−8224

upon layer number. Local differences in layer number arising from step edges (single to few layer) or terraces (multilayer) can reasonably be expected to impact the overall dynamics, as the total transit times of the interlayer mode between the outer layers will differ. Such a response is hypothesized to produce a localized spatiotemporal dephasing of the interlayer mode soon after fs photoexcitation with the discrete responses separated by the structural discontinuity. Recall that contrast features oscillating about a fixed spatial position in the UEM bright-field image series arises from excitation of the interlayer mode. Thus, analysis of such features enables quantification of the speed of the structural perturbation when the thickness is known (see Figure 2). Here, such behaviors were directly observed with UEM by monitoring two discrete bend contours separated by a crystal step edge within a specific ROI (Figure 4). These specific features (labeled 1 and 2 in Figure 4a) were located within the $\vec{k}_i \angle [001] = 40°$ crystal section. Spatial FFT maps of this ROI (Figure 4b) reveal the locations of the discrete oscillation frequencies present in the STCPs in Figure 2d,e (56.7 and 63.3 GHz). Each structural oscillation is readily observable by quantifying the motion of each bend contour via individual STCPs (Figure 4c−e).

As can be seen from Figure 4, the two bend contours monitored in this region display distinct oscillation frequencies differing by 6.6 GHz, as noted above. The temporal aspects of this can be visualized in the STCPs, with the difference in oscillation frequencies appearing as an increasing phase shift with time. For example, the second peak of the first oscillation period of bend contour 1 occurs 16.5 ps after initial motion, whereas that of bend contour 2 occurs after 15.4 ps. For the fifth period, however, the difference has increased from 1.1 to 5.5 ps. Such a lag is indicative of a slight difference in layer number at the locations of the individual bend contours (i.e., a difference in total transit time of the strain waves between the outer layers). Taking the speed of the interlayer mode to be 2.9 nm/ps, the difference between these two regions is four MoS_2 layers (i.e., two unit-cell lengths along the principal *c*-axis stacking direction). Such a few-layer picosecond dephasing is readily apparent in the UEM image series (see Supporting Videos 1 and 2); the two bend contours initially appear to move in unison but quickly go out of phase and appear to oscillate independent of one another. The presence of a few-layer step edge running between the two bend contours can also be seen with high-angle annular dark-field scanning transmission electron microscopy (HAADF-STEM) imaging and by close inspection of specific still frames in the UEM image series (see the Supporting Information and Figure S6). In the HAADF-STEM image, the step edge appears as a slight change in counts due to the difference in thickness; the slightly thicker region (i.e., the region displaying the lower 56.7 GHz oscillation frequency) appears bright relative to the thinner region. In select UEM bright-field images, indication of the presence of the edge is more subtle and appears as a spatial discontinuity in the bend contour. Note that the 60.0 GHz signal in the spatial FFT in Figure 4b occurs mainly at the step edge position and is likely due to a convolution of the 56.7 and 63.3 GHz signals (i.e., it is exactly the average of those two signals), though it is possible it instead arises from the presence of an unresolved single-layer step edge. In addition to revealing the sensitivity of the structural dynamics to subtle variations in local structure and morphology, observation of this localized dephasing behavior further demonstrates the usefulness of UEM real-space imaging for elucidating detailed structural responses on the combined nanometer−picosecond spatio-temporal scales.

In summary, the interconnectedness of photoexcited intra-layer and interlayer strain-wave modes in multilayer 2H-MoS_2, and especially with respect to structural discontinuities, has been studied with fs electron imaging in an ultrafast electron microscope. With direct, real-space imaging on combined nanometer−picosecond scales, and by studying a crystal specimen that provided access to 3D structural information, it was found that both modes could be observed within a single 2D projection image series (i.e., there was no need to tilt the specimen or the incident beam and conduct different measurements in order to access the two distinct modes). In this way, the mode velocities were determined, and a time lag of 2.4 ps between the intralayer and interlayer modes was observed. On the basis of this, a mechanism was proposed involving initiation of the propagating, in-plane mode by enhanced freedom of motion of basal-plane edges forming a discrete terrace. The combination of motion along the *c*-axis direction and symmetry breaking at the terrace leads to excitation of transient ripples that propagate within the *ab* plane and initially away from the defect. This was supported by observation of a picosecond dephasing of the oscillatory behavior of two distinct bend contours separated by a four-layer crystal step edge. In addition to uncovering new fundamental behaviors, these results could potentially inform applications in, for example, tunable optoelectronics requiring high sensitivity and precision.

■ ASSOCIATED CONTENT

Supporting Information

The Supporting Information is available free of charge on the ACS Publications website at DOI: 10.1021/acs.nanolett.9b03596.

Materials and Methods include methods in determining the thickness of the specimen of interest, extraction of the intralayer strain-wave speed, calculation of the interlayer strain-wave speed, differentiation of the intralayer and interlayer strain-wave speeds, determination of bend-contour position from STCPs, and confirmation of the presence of a crystal step edge as the source of interlayer dephasing; supporting tables display the extracted and calculated intralayer and interlayer strain-wave speeds, and the elastic constants used to calculate the speeds; supporting figures and additional references (PDF)

UEM bright-field video of picosecond photoinduced strain-wave dynamics in multilayer MoS_2 (AVI)

UEM difference image video of Supporting Video 1 (AVI)

■ AUTHOR INFORMATION

Corresponding Author

*E-mail: flan0076@umn.edu. Office: +1 612-625-3867.

ORCID

David J. Flannigan: 0000-0002-1829-1868

Author Contributions

Y.Z. contributed formal analysis, investigation, methodology, software, validation, visualization, writing the original draft, reviewing, and editing. D.J.F. contributed conceptualization, formal analysis, funding acquisition, methodology, project

DOI: 10.1021/acs.nanolett.9b03596
Nano Lett. 2019, 19, 8216−8224

administration, resources, supervision, visualization, writing the original draft, reviewing, and editing.

Funding

This material is based upon work supported by the National Science Foundation under Grant DMR-1654318. This work was supported partially by the National Science Foundation through the University of Minnesota MRSEC under Award Number DMR-1420013. Part of this work was carried out in the College of Science and Engineering Characterization Facility, University of Minnesota, which has received capital equipment funding from the NSF through the UMN MRSEC program under Award Numbers DMR-0819885 and DMR-1420013.

Notes

The authors declare no competing financial interest.

■ ACKNOWLEDGMENTS

We thank Ryan Gnabasik for discussions related to determining the time delay between the onsets of the interlayer and intralayer dynamics from the UEM imaging data.

■ REFERENCES

(1) Bertolazzi, S.; Brivio, J.; Kis, A. Stretching and breaking of ultrathin MoS_2. *ACS Nano* **2011**, *5*, 9703−9709.
(2) Castellanos-Gomez, A.; Poot, M.; Steele, G. A.; van der Zant, H. S. J.; Agrait, N.; Rubio-Bollinger, G. Elastic properties of freely suspended MoS_2 nanosheets. *Adv. Mater.* **2012**, *24*, 772−775.
(3) Yun, W. S.; Han, S. W.; Hong, S. C.; Kim, I. G.; Lee, J. D. Thickness and strain effects on electronic structures of transition metal dichalcogenides: 2H-M_2 semiconductors (M = Mo, W; X = S, Se, Te). *Phys. Rev. B: Condens. Matter Mater. Phys.* **2012**, *85*, 033305.
(4) Johari, P.; Shenoy, V. B. Tuning the electronic properties of semiconducting transition metal dichalcogenides by applying mechanical strains. *ACS Nano* **2012**, *6*, 5449−5456.
(5) Conley, H. J.; Wang, B.; Ziegler, J. I.; Haglund, R. F.; Pantelides, S. T.; Bolotin, K. I. Bandgap engineering of strained monolayer and bilayer MoS_2. *Nano Lett.* **2013**, *13*, 3626−3630.
(6) Castellanos-Gomez, A.; Roldán, R.; Cappelluti, E.; Buscema, M.; Guinea, F.; van der Zant, H. S. J.; Steele, G. A. Local strain engineering in atomically thin MoS_2. *Nano Lett.* **2013**, *13*, 5361−5366.
(7) Liu, K.; Zhang, L.; Cao, T.; Jin, C.; Qiu, D.; Zhou, Q.; Zettl, A.; Yang, P.; Louie, S. G.; Wang, F. Evolution of interlayer coupling in twisted molybdenum disulfide bilayers. *Nat. Commun.* **2014**, *5*, 4966.
(8) Huang, S.; Ling, X.; Liang, L.; Kong, J.; Terrones, H.; Meunier, V.; Dresselhaus, M. S. Probing the interlayer coupling of twisted bilayer MoS_2 using photoluminescence spectroscopy. *Nano Lett.* **2014**, *14*, 5500−5508.
(9) Yang, S.; Wang, C.; Sahin, H.; Chen, H.; Li, Y.; Li, S.-S.; Suslu, A.; Peeters, F. M.; Liu, Q.; Li, J.; Tongay, S. Tuning the optical, magnetic, and electrical properties of $ReSe_2$ by nanoscale strain engineering. *Nano Lett.* **2015**, *15*, 1660−1666.
(10) Lloyd, D.; Liu, X.; Christopher, J. W.; Cantley, L.; Wadehra, A.; Kim, B. L.; Goldberg, B. B.; Swan, A. K.; Bunch, J. S. Band gap engineering with ultralarge biaxial strains in suspended monolayer MoS_2. *Nano Lett.* **2016**, *16*, 5836−5841.
(11) Kumar, S.; Kaczmarczyk, A.; Gerardot, B. D. Strain-induced spatial and spectral isolation of quantum emitters in mono- and bilayer WSe_2. *Nano Lett.* **2015**, *15*, 7567−7573.
(12) Aslan, O. B.; Datye, I. M.; Mleczko, M. J.; Sze Cheung, K.; Krylyuk, S.; Bruma, A.; Kalish, I.; Davydov, A. V.; Pop, E.; Heinz, T. F. Probing the optical properties and strain-tuning of ultrathin $Mo_{1-x}W_xTe_2$. *Nano Lett.* **2018**, *18*, 2485−2491.
(13) Wang, Q. H.; Kalantar-Zadeh, K.; Kis, A.; Coleman, J. N.; Strano, M. S. Electronics and optoelectronics of two-dimensional transition metal dichalcogenides. *Nat. Nanotechnol.* **2012**, *7*, 699−712.
(14) Koperski, M.; Nogajewski, K.; Arora, A.; Cherkez, V.; Mallet, P.; Veuillen, J. Y.; Marcus, J.; Kossacki, P.; Potemski, M. Single photon emitters in exfoliated WSe_2 structures. *Nat. Nanotechnol.* **2015**, *10*, 503−506.
(15) Srivastava, A.; Sidler, M.; Allain, A. V.; Lembke, D. S.; Kis, A.; Imamoğlu, A. Optically active quantum dots in monolayer WSe_2. *Nat. Nanotechnol.* **2015**, *10*, 491−496.
(16) Tonndorf, P.; Schmidt, R.; Schneider, R.; Kern, J.; Buscema, M.; Steele, G. A.; Castellanos-Gomez, A.; van der Zant, H. S. J.; Michaelis de Vasconcellos, S.; Bratschitsch, R. Single-photon emission from localized excitons in an atomically thin semiconductor. *Optica* **2015**, *2*, 347−352.
(17) Kern, J.; Niehues, I.; Tonndorf, P.; Schmidt, R.; Wigger, D.; Schneider, R.; Stiehm, T.; Michaelis de Vasconcellos, S.; Reiter, D. E.; Kuhn, T.; Bratschitsch, R. Nanoscale positioning of single-photon emitters in atomically thin WSe_2. *Adv. Mater.* **2016**, *28*, 7101−7105.
(18) Plechinger, G.; Heydrich, S.; Eroms, J.; Weiss, D.; Schüller, C.; Korn, T. Raman spectroscopy of the interlayer shear mode in few-layer MoS_2 flakes. *Appl. Phys. Lett.* **2012**, *101*, 101906.
(19) Zhao, Y.; Luo, X.; Li, H.; Zhang, J.; Araujo, P. T.; Gan, C. K.; Wu, J.; Zhang, H.; Quek, S. Y.; Dresselhaus, M. S.; Xiong, Q. Interlayer breathing and shear modes in few-trilayer MoS_2 and WSe_2. *Nano Lett.* **2013**, *13*, 1007−1015.
(20) Mannebach, E. M.; Li, R.; Duerloo, K.-A.; Nyby, C.; Zalden, P.; Vecchione, T.; Ernst, F.; Reid, A. H.; Chase, T.; Shen, X.; Weathersby, S.; Hast, C.; Hettel, R.; Coffee, R.; Hartmann, N.; Fry, A. R.; Yu, Y.; Cao, L.; Heinz, T. F.; Reed, E. J.; Dürr, H. A.; Wang, X.; Lindenberg, A. M. Dynamic structural response and deformations of monolayer MoS_2 visualized by femtosecond electron diffraction. *Nano Lett.* **2015**, *15*, 6889−6895.
(21) Cremons, D. R.; Plemmons, D. A.; Flannigan, D. J. Femtosecond electron imaging of defect-modulated phonon dynamics. *Nat. Commun.* **2016**, *7*, 11230.
(22) Cremons, D. R.; Plemmons, D. A.; Flannigan, D. J. Defect-mediated phonon dynamics in TaS_2 and WSe_2. *Struct. Dyn.* **2017**, *4*, 044019.
(23) McKenna, A. J.; Eliason, J. K.; Flannigan, D. J. Spatiotemporal evolution of coherent elastic strain waves in a single MoS_2 flake. *Nano Lett.* **2017**, *17*, 3952−3958.
(24) Mannebach, E. M.; Nyby, C.; Ernst, F.; Zhou, Y.; Tolsma, J.; Li, Y.; Sher, M.-J.; Tung, I. C.; Zhou, H.; Zhang, Q.; Seyler, K. L.; Clark, G.; Lin, Y.; Zhu, D.; Glownia, J. M.; Kozina, M. E.; Song, S.; Nelson, S.; Mehta, A.; Yu, Y.; Pant, A.; Aslan, O. B.; Raja, A.; Guo, Y.; DiChiara, A.; Mao, W.; Cao, L.; Tongay, S.; Sun, J.; Singh, D. J.; Heinz, T. F.; Xu, X.; MacDonald, A. H.; Reed, E.; Wen, H.; Lindenberg, A. M. Dynamic optical tuning of interlayer interactions in the transition metal dichalcogenides. *Nano Lett.* **2017**, *17*, 7761−7766.
(25) Waldecker, L.; Bertoni, R.; Hübener, H.; Brumme, T.; Vasileiadis, T.; Zahn, D.; Rubio, A.; Ernstorfer, R. Momentum-resolved view of electron-phonon coupling in multilayer WSe_2. *Phys. Rev. Lett.* **2017**, *119*, 036803.
(26) Kim, T.; Ding, D.; Yim, J.-H.; Jho, Y.-D.; Minnich, A. J. Elastic and thermal properties of free-standing molybdenum disulfide membranes measured using ultrafast transient grating spectroscopy. *APL Mater.* **2017**, *5*, 086105.
(27) Reisbick, S. A.; Flannigan, D. J. Correlating atomic-scale lattice and nanoscale structural dynamics with ultrafast electron microscopy. *Microsc. Microanal.* **2019**, *25*, 950−951.
(28) Krishnamoorthy, A.; Lin, M.-F.; Zhang, X.; Weninger, C.; Ma, R.; Britz, A.; Tiwary, C. S.; Kochat, V.; Apte, A.; Yang, J.; Park, S.; Li, R.; Shen, X.; Wang, X.; Kalia, R.; Nakano, A.; Shimojo, F.; Fritz, D.; Bergmann, U.; Ajayan, P.; Vashishta, P. Optical control of non-equilibrium phonon dynamics. *Nano Lett.* **2019**, *19*, 4981−4989.
(29) Chiritescu, C.; Cahill, D. G.; Nguyen, N.; Johnson, D.; Bodapati, A.; Keblinski, P.; Zschack, P. Ultralow thermal conductivity in disordered, layered WSe_2 crystals. *Science* **2007**, *315*, 351−353.
(30) Yazyev, O. V.; Louie, S. G. Electronic transport in polycrystalline graphene. *Nat. Mater.* **2010**, *9*, 806−809.

DOI: 10.1021/acs.nanolett.9b03596
Nano Lett. 2019, 19, 8216−8224

(31) Serov, A. Y.; Ong, Z.-Y.; Pop, E. Effect of grain boundaries on thermal transport in graphene. *Appl. Phys. Lett.* **2013**, *102*, 033104.
(32) Fei, Z.; Rodin, A. S.; Gannett, W.; Dai, S.; Regan, W.; Wagner, M.; Liu, M. K.; McLeod, A. S.; Dominguez, G.; Thiemens, M.; Castro Neto, A. H.; Keilmann, F.; Zettl, A.; Hillenbrand, R.; Fogler, M. M.; Basov, D. N. Electronic and plasmonic phenomena at graphene grain boundaries. *Nat. Nanotechnol.* **2013**, *8*, 821−825.
(33) Zhang, H.; Lee, G.; Gong, C.; Colombo, L.; Cho, K. Grain boundary effect on electrical transport properties of graphene. *J. Phys. Chem. C* **2014**, *118*, 2338−2343.
(34) Huang, Y. L.; Chen, Y.; Zhang, W.; Quek, S. Y.; Chen, C.-H.; Li, L.-J.; Hsu, W.-T.; Chang, W.-H.; Zheng, Y. J.; Chen, W.; Wee, A. T. S. Bandgap tunability at single-layer molybdenum disulphide grain boundaries. *Nat. Commun.* **2015**, *6*, 6298.
(35) Brivio, J.; Alexander, D. T. L.; Kis, A. Ripples and layers in ultrathin MoS_2 membranes. *Nano Lett.* **2011**, *11*, 5148−5153.
(36) Ataca, C.; Şahin, H.; Aktürk, E.; Ciraci, S. Mechanical and electronic properties of MoS_2 nanoribbons and their defects. *J. Phys. Chem. C* **2011**, *115*, 3934−3941.
(37) Qi, J.; Li, X.; Qian, X.; Feng, J. Bandgap engineering of rippled MoS_2 monolayer under external electric field. *Appl. Phys. Lett.* **2013**, *102*, 173112.
(38) Miró, P.; Ghorbani-Asl, M.; Heine, T. Spontaneous ripple formation in MoS_2 monolayers: Electronic structure and transport effects. *Adv. Mater.* **2013**, *25*, 5473−5475.
(39) KC, S.; Longo, R. C.; Addou, R.; Wallace, R. M.; Cho, K. Impact of intrinsic atomic defects on the electronic structure of MoS_2 monolayers. *Nanotechnology* **2014**, *25*, 375703.
(40) Luo, S.; Hao, G.; Fan, Y.; Kou, L.; He, C.; Qi, X.; Tang, C.; Li, J.; Huang, K.; Zhong, J. Formation of ripples in atomically thin MoS_2 and local strain engineering of electrostatic properties. *Nanotechnology* **2015**, *26*, 105705.
(41) Addou, R.; Colombo, L.; Wallace, R. M. Surface defects on natural MoS_2. *ACS Appl. Mater. Interfaces* **2015**, *7*, 11921−11929.
(42) Mills, A.; Yu, Y.; Chen, C.; Huang, B.; Cao, L.; Tao, C. Ripples near edge terminals in MoS_2 few layers and pyramid nanostructures. *Appl. Phys. Lett.* **2016**, *108*, 081601.
(43) Hong, J.; Hu, Z.; Probert, M.; Li, K.; Lv, D.; Yang, X.; Gu, L.; Mao, N.; Feng, Q.; Xie, L.; Zhang, J.; Wu, D.; Zhang, Z.; Jin, C.; Ji, W.; Zhang, X.; Yuan, J.; Zhang, Z. Exploring atomic defects in molybdenum disulphide monolayers. *Nat. Commun.* **2015**, *6*, 6293.
(44) Vancsó, P.; Magda, G. Z.; Pető, J.; Noh, J.-Y.; Kim, Y.-S.; Hwang, C.; Biró, L. P.; Tapasztó, L. The intrinsic defect structure of exfoliated MoS_2 single layers revealed by scanning tunneling microscopy. *Sci. Rep.* **2016**, *6*, 29726.
(45) Hovden, R.; Liu, P.; Schnitzer, N.; Tsen, A. W.; Liu, Y.; Lu, W.; Sun, Y.; Kourkoutis, L. F. Thickness and stacking sequence determination of exfoliated dichalcogenides (1T-TaS_2, 2H-MoS_2) using scanning transmission electron microscopy. *Microsc. Microanal.* **2018**, *24*, 387−395.
(46) Nie, Z.; Long, R.; Sun, L.; Huang, C.-C.; Zhang, J.; Xiong, Q.; Hewak, D. W.; Shen, Z.; Prezhdo, O. V.; Loh, Z.-H. Ultrafast carrier thermalization and cooling dynamics in few-layer MoS_2. *ACS Nano* **2014**, *8*, 10931−10940.
(47) Plemmons, D. A.; Suri, P. K.; Flannigan, D. J. Probing structural and electronic dynamics with ultrafast electron microscopy. *Chem. Mater.* **2015**, *27*, 3178−3192.
(48) Barwick, B.; Park, H. S.; Kwon, O. H.; Baskin, J. S.; Zewail, A. H. 4D imaging of transient structures and morphologies in ultrafast electron microscopy. *Science* **2008**, *322*, 1227−1231.
(49) Kwon, O.-H.; Barwick, B.; Park, H. S.; Baskin, J. S.; Zewail, A. H. Nanoscale mechanical drumming visualized by 4D electron microscopy. *Nano Lett.* **2008**, *8*, 3557−3562.
(50) Flannigan, D. J.; Zewail, A. H. Optomechanical and crystallization phenomena visualized with 4D electron microscopy: Interfacial carbon nanotubes on silicon nitride. *Nano Lett.* **2010**, *10*, 1892−1899.
(51) Feldman, J. L. Elastic constants of 2H-MoS_2 and 2H-$NbSe_2$ extracted from measured dispersion curves and linear compressibilities. *J. Phys. Chem. Solids* **1976**, *37*, 1141−1144.
(52) Alexiev, V.; Prins, R.; Weber, T. *Ab initio* study of MoS_2 and Li adsorbed on the (1010) face of MoS_2. *Phys. Chem. Chem. Phys.* **2000**, *2*, 1815−1827.
(53) Todorova, T.; Alexiev, V.; Prins, R.; Weber, T. *Ab initio* study of 2H-MoS_2 using Hay and Wadt effective core pseudo-potentials for modelling the (1010) surface structure. *Phys. Chem. Chem. Phys.* **2004**, *6*, 3023−3030.
(54) Peelaers, H.; Van de Walle, C. G. Elastic constants and pressure-induced effects in MoS_2. *J. Phys. Chem. C* **2014**, *118*, 12073−12076.
(55) Kumazoe, H.; Krishnamoorthy, A.; Bassman, L.; Kalia, R. K.; Nakano, A.; Shimojo, F.; Vashishta, P. Photo-induced lattice contraction in layered materials. *J. Phys.: Condens. Matter* **2018**, *30*, 32LT02.

DOI: 10.1021/acs.nanolett.9b03596
Nano Lett. 2019, 19, 8216−8224